Tunneling nanotubes propagate a BMP-dependent preneoplastic state.

Cristina Cuella Martin[1,2,3], Thanh Thuy Nguyen[1,2,3] *, Alexia Bertin[1,2,3] *, Kevin Geistlich[1,2,3,4], Boris Guyot[1,2,3], Sylvain Lefort[1,2,3], Emmanuel Delay[1,2,3,4], Charline Dalverny[3,5], Alice Boissard[6], Cécile Henry[6], François Guillonneau[6,7,8],

Eve-Isabelle Pécheur[1,2,3§]* and Véronique Maguer-Satta[1,2,3,4 §]*

1. CNRS UMR5286, Centre de Recherche en Cancérologie de Lyon, 69008 Lyon, France; 2. Inserm U1052, Centre de Recherche en Cancérologie de Lyon, 69008 Lyon, France; 3. Université Claude Bernard Lyon 1, Lyon, France; 4. Centre Léon Bérard, 69008 Lyon, France; 5. Centre Technologique des Microstructures, 69622 Villeurbanne, France; 6. Prot'ICO proteomics facility, Institut de Cancérologie de l'Ouest, 49055 Angers, France, 7. Nantes Université, Inserm, CNRS, CRCI2NA, U1307, UMR6075, 44000 Nantes, France; 8. Equipe Labellisée Ligue Contre le Cancer, Paris, France.

* These authors contributed equally; [§] Co-corresponding authors

Co-corresponding authors: Eve-Isabelle PÉCHEUR and Véronique MAGUER-SATTA, Centre de Recherche en Cancérologie de Lyon-CRCL, UMR CNRS 5286/Inserm U1052, 28 rue Laënnec, 69373 Lyon Cedex 08, France; 33-4-7878-2907 or 33-4-7878-2806. Emails: **eve-isabelle.pecheur@inserm.fr** ; **veronique.maguer-satta@lyon.unicancer.fr**

Keywords: Tunneling nanotubes, cell communication, preneoplasia, BMP, luminal breast tumor initiation, stem cells.

Abstract.

Tunneling nanotubes (TNTs) are thin, actin-based structures allowing long-distance communication between cells by promoting the transfer of molecules and organelles. Well-known to contribute to cancer progression, we investigated their role in early tumor initiation using an in-house human breast cell model recapitulating early transformation. We observed that TNTs become more abundant and elongated during this process, and preferentially connect transformed donor cells to non-transformed acceptor cells. We show that this long-range, directional communication involves the transfer of the signaling receptor BMPR1b. Within days, this transfer induces gene expression changes in acceptor cells, consistent with early transformation programs. Functional analyses of these acceptor cells revealed metabolic rewiring and phenotypic changes, including anchorage-independent growth. Moreover, the transferred BMPR1b receptor sensitized acceptor cells to BMP2 signals present in the microenvironment, amplifying their transformation potential. Hence, by tracking the earliest molecular responses in acceptor cells, we deciphered the initial steps of a transformation cascade triggered by TNT-mediated transfer. These findings uncover a BMP-dependent mechanism by which transformed cells propagate a preneoplastic state to adjacent cells at the onset of transformation, offering new perspectives on how epithelial transformation arises and spreads to neighboring cells.

Cell-cell interactions are critical in cancer development, impacting tumor growth, invasion, and metastasis. Within the cancer ecosystem, various cell types, including neurons, fibroblasts and immune cells, interact with cancer cells through direct contacts and soluble factors, fostering tumor progression and immune evasion[1,2]. In particular, stem cells within tumors rely on interactions with their surrounding cellular and non-cellular environment for their survival and functioning[3,4]. Indeed, cancer stem cells can drive tumorigenesis and resistance to therapy through exogenous signaling pathways that maintain their stemness and promote survival[5]. Intercellular communication through gap junctions and exosomes allows the transfer of molecules that can either suppress or promote cancer, depending on the context[5]. Deciphering how cells communicate during the earliest stages of transformation is critical for identifying new therapeutic targets that can disrupt pro-tumorigenic signaling and halt tumor progression. Yet, the nature, directionality, and functional consequences of cell-to-cell communications at this stage remain largely undetermined.

Tunneling nanotubes (TNTs) are thin, transient actin-based structures that enable direct long-range communication between cells[6,7,8]. TNTs mediate the transfer of organelles, proteins, and nucleic acids, and have been implicated in cancer progression, metastasis, and resistance to therapy. Recent findings suggest that TNTs can enhance cancer cell metabolism and dissemination, notably through mitochondrial transfer from neurons[2,9,10]. Despite growing interest, TNTs remain poorly characterized at the molecular level, lacking specific markers and mechanistic understanding. Their presence has been documented in various cancer models and patient-derived samples, yet their role in the earliest stages of tumorigenesis remains largely unexplored. Addressing this knowledge gap is essential to uncover how intercellular communications contribute to transformation and to identify new therapeutic strategies targeting early pro-tumorigenic interactions.

In the context of stem cell transformation, we previously identified the bone morphogenetic protein (BMP) as a key driver of luminal breast cancer, capable of inducing the transformation of immature mammary cells[11,12]. Our group and others have shown that BMP signaling regulates cancer stem cell maintenance across various tumors types[13–15]. In luminal breast cancer, fueled by IL6-dependent inflammation, we found that excessive BMP2 secretion from the tumor microenvironment, initiates stem cell transformation towards a luminal tumor-like phenotype via the BMP type 1b receptor (BMPR1b), without inducing detectable genetic alterations[13,15]. The BMP signaling pathway has also been linked to tumor cell dissemination and chemoresistance in several cancers, including breast cancer[16]. However, the early dynamics of BMP-mediated transformation and their evolution towards fully transformed tumor cells remain unexplored. Moreover, while BMPs and TNTs have independently been associated with breast cancer metastasis and resistance to therapy, their potential interaction and the role of TNTs in early tumorigenesis are still unknown.

Here, we investigated the mechanisms driving the earliest steps of transformation in immature mammary cells, using normal human primary mammary cells and a unique cell line model that recapitulates early transformation[12]. We found that the number of TNTs increases, that they are more elongated during transformation, and that they preferentially connect transformed donor cells to non-transformed acceptor cells. These directional, long-range contacts enable the transfer of cellular information, triggering preneoplastic changes in acceptor cells. We further identified BMPR1b as a central regulator of TNT formation and elongation.

Altogether, our study uncovers a previously unrecognized interplay between the BMP signaling pathway and TNT-mediated communication, revealing how transformed cells can initiate and propagate early tumorigenic signals to neighboring cells during mammary tumor initiation.

Transformation of mammary epithelial stem cells enhances TNT formation and elongation. To explore early BMP-driven transformation dynamics, we used MCF10A-derived stem cells models obtained by chronic exposure to IL6 and BMP2 (MC26 and M1B26; Fig. 1a). The sorting of MCF10A cells expressing BMPR1b prior to cytokine treatment, followed by the selection of soft agar clones, led to the quicker establishment of transformed cells (M1B26), with greater *in vitro* anchorage-independent growth and *in vivo* engraftment than in non BMPR1b-sorted cells (MC26)[13,15]. As shown previously, these models recapitulate early *in vivo* alterations of the BMP pathway and display molecular features of ductal carcinoma *in situ*, providing a robust system to investigate the dynamics of early transformation in immature mammary cells[13,15]. Confocal microscopy observations of non-transformed control (MCF10A-CT) and transformed cells (MC26, M1B26) revealed that distant cells established contacts *via* long and thin F-actin-rich membrane TNTs (tunneling nanotubes)[17] (Fig. 1b). Although TNT quantification requires low-confluence cultures[18], long-range TNTs were also detectable at high cell density (Extended Data Fig. 1a). Transformed cells exhibited over twice as many TNTs as non-transformed cells (Fig. 1c, left panel). The proportion of long TNTs increased nearly fivefold with transformation, rising significantly to around 10% in M1B26 cells (Fig. 1c, right panel). Even though their numbers augmented significantly, the average length of TNTs did not differ significantly between cell lines (Extended Data Fig 1b). Interestingly, neither the number nor length of TNTs varied in non-transformed cells exposed to conditioned medium of transformed ones (Extended Data Fig. 1b,c,d). In agreement with previous data[6,17], TNTs in transformed cells were often branched with numerous ramifications, and displayed bulges visible by scanning electron microscopy (Fig. 1d black arrow). While most TNTs were open-ended, allowing a continuous cytoplasmic connection between cells (Fig. 1e), we also observed some close-ended TNTs featuring a Gap junction at one tip (Extended data Fig.1e). Notably, TNTs did not adhere to the substrate and could also be observed within 3D structures such as acini, the basic functional units of breast glandular tissue (Fig. 1f; Extended Data Fig.1f). TNTs

also contained microtubules[6,19] (Extended Data Fig.1g), and mitochondria that seemed to traffic between cells (Fig. 1g; Extended Data Fig.1h). Importantly, transformed cells (M1B26) could also connect through TNTs to non-transformed primary fibroblasts (Fig. 1h) or epithelial mammary cells (Fig. 1i) isolated from healthy human breast samples.

Taken together, these data indicate that early transformation of mammary immature cells leads to an enhanced ability of transformed cells to connect to neighboring cells through TNTs, and to transfer material, such as mitochondria.

Directional transfer of cellular material *via* TNTs from transformed to non-transformed cells.

To investigate how TNTs connect cells, we performed cocultures using fluorescent mCherry- or GFP-tagged MCF10A-CT or M1B26 cells, respectively. Cells were seeded at low density, to minimize direct cell-cell membrane contacts. We observed that both M1B26 transformed (Tf) and MCF10A-CT non-transformed (NoTf) cells were able to extend TNT structures, connecting Tf to Tf, NoTf to NoTf and Tf to NoTf cells (Fig. 2a). Quantification of the different types of TNT contacts revealed that connections were more frequent and abundant from Tf cells towards NoTf cells than in the opposite direction (Fig. 2b,c). Fluorescent material originating from GFP-tagged Tf cells accumulated within the cytoplasm of NoTf cells (Fig. 2d), suggesting a directional transfer *via* TNTs, with Tf cells acting as donors and NoTf cells as acceptors. This was further confirmed using time-lapse microscopy analysis (see Extended data Movie 1, Fig. 2e and Extended Data Fig. 2a). To assess the proportion of cellular exchange between cells, mCherry-NoTf cells were cocultured at low density with GFP-Tf cells for 8 days. Flow cytometry analysis revealed a higher proportion of mCherry-NoTf cells exhibiting green fluorescence uptake compared to GFP-Tf cells acquiring red fluorescence (Extended data Fig. 2b), indicating a preferential transfer of fluorescent material from Tf to NoTf cells (Fig. 2f,g). Moreover, the intensity of transferred fluorescence was higher in the Tf-to-NoTf direction (Fig. 2h), and switching fluorophores between Tf and NoTf cells

yielded similar results (Extended data Fig. 2c,d). Of note, the directional transfer from Tf to NoTf cells increased over time in coculture, independently of the fluorophore used (Extended data Fig. 2e-i). When using mCherry-labeled normal human primary mammary cells as the source of NoTf cells, we also observed a directional transfer of material from Tf to these NoTf cells in coculture (Fig. 2j,k), observed with NoTf MCF10A-CT cells as well (Extended Data Fig. 2j). Since cells also communicate by exchanging soluble materials and extracellular vesicles, we carried out 8-day cultures of the normal human primary and Tf cells separated by a physical barrier to prevent TNT formation (Transwell™), as well as cultures of normal human primary cells in the conditioned medium of Tf cells (schematic, Fig. 2i). When TNT formation was physically impeded, the number of acceptor cells dropped in both directions of the transfer (Fig. 2j,k; Extended Data Fig. 2j). No fluorescence exchange *via* soluble components in conditioned medium (CM) experiments was observed, as also confirmed by fluorescence intensity measurements (Extended Data Fig. 2k,l). Altogether, these data indicate that directional transfer of material preferentially occurs *via* TNTs rather than through other forms of cell-cell communication, and mainly from Tf to NoTf cells.

TNT-mediated transfer modulates metabolic and phenotypic features of acceptor cells.

Fluorescent-labeled cells, cultured for 8 days under the conditions described in Fig. 3a, were sorted by flow cytometry into four populations: non-transformed (NoTf), transformed (Tf), non-transformed cells that received fluorescent material (NoTf accept), and non-transformed cells that did not (NoTf no accept). Proteomic analysis of each population followed by gene enrichment pathway analysis revealed that the most enriched pathways in NoTf accept cells, compared to NoTf non-acceptor cells, were primarily related to mitochondrial structure and activity (including respiratory chain assembly, aerobic respiration and oxidative phosphorylation), various transport processes (transmembrane, intracellular, ion, nitrogen compound and macro-molecule transport), as well as organelle and protein localization in the cell (Fig. 3b). Volcano plot analysis revealed

that NoTf accept were statistically distinct from NoTf and NoTf no accept cells (Fig. 3c and Extended Data Fig. 3a). Of note, the most overexpressed proteins in the former phenotype were involved in mitochondrial-related processes (respiration, glycolysis, oxidative phosphorylation genes, including *SLC25A51, SLC25A52, COX6C, COX7C*; mitochondrial ribosome biogenesis, such as *MALSU1*). This is consistent with a metabolic rewiring that may be at least partly driven by the transfer of mitochondria from Tf to NoTf cells which are abundantly present within TNTs (Fig. 1g; Extended Data Fig. 1h, 3b). Increased protein expression was observed for proteins involved in lipid metabolism and transport (*ATP8B1, RAB6B, CES1* – EST1*, PIGA*), intracellular membrane and secretory vesicle trafficking (*RAB6B, RAB11B, SYT8, CAV2, TMEM167A*), cell growth and maintenance of cell morphology (*TRIQK*), microvillus/membrane protrusion formation (*ATP8B1*) and actin filament bundling (*LCP1* – Plastin-2) (Table S1). The level of four proteins, namely EST1/*CES1*, Plastin-2/*LCP1*, Rab-6B, and TRIQK, was markedly increased in NoTf accept compared to NoTf no accept cells. (Fig. 3d). Interestingly, RNA levels of the genes encoding these proteins were enhanced in Tf compared to NoTf cells (Extended Data Fig. 3c). These findings suggest that the transfer of material induces transcriptional and translational upregulation of key proteins in acceptor cells, thereby promoting their progression towards a transformed-like phenotype. Concomitantly, among the proteins showing the lowest levels were DAP1 (*DAP*) and thymosin β-10 (*TMSB10*), respectively involved in ribosome hibernation, thereby preventing mRNA translation, and in inhibiting actin polymerization (Table S1).

When TNT formation was physically blocked using Transwell™ inserts, acceptor cells grown in this context showed phenotypic differences compared to those in direct coculture (Table S2), but remained similar to NoTf cells (Extended Data Fig. 3d,e). Notably, NoTf accept cells from direct cocultures exhibited a higher expression of early inflammatory markers (*SERPINA3, CD14*) and motility-related genes (*IGFBP6*) than their Transwell counterparts. These findings indicate that: (i) direct contact with transformed cells *via* TNTs induces metabolic, energetic, and structural changes

in non-transformed acceptor cells, resembling early oncogenic transformation; and (ii) these alterations are primarily driven by TNT-mediated directional transfer. Given that Ras-driven oncogenic transformation is a well-established process, we next investigated whether such BMP-independent transformation could promote the formation of long tunneling nanotubes (TNTs). To this end, we first assessed the expression of H-Ras and K-Ras in our system. Proteomic analysis revealed a marked increase in both oncoproteins in NoTf accept cells compared to NoTf cells (Fig. 3e). To further assess a potential link between Ras-induced transformation and TNT formation, we examined two additional models. First, in the Weinberg model using HMLER cells (HMEC immortalized with SV40-L and hTERT, then transformed with H-Ras)[20], TNTs were present in both malignant and non-malignant cells, with shorter TNTs in HMLER compared to HMLE cells (Fig. 3f,h). Second, in H-Ras-transformed MCF10A-derived AT1 and DCIS cells, malignant cells exhibited fewer TNTs than non-malignant ones, with no difference in TNT length (Fig. 3g,i). This supports that Ras-induced transformation does not enhance long-distance TNT-mediated communication.

In summary, TNT-mediated transfer induces metabolic rewiring and upregulation of transformation-associated transcripts and proteins in non-transformed acceptor cells. In contrast, Ras-driven transformation does not promote the formation of long TNTs nor long-distance TNT-mediated communication, underscoring the specificity of BMP/inflammation-driven mechanisms.

BMP signaling drives TNT-mediated preneoplastic reprogramming.

To further investigate the interplay between BMP signaling, TNT structures, and preneoplastic reprogramming, gene ontology biological process (GOBP) enrichment analysis was performed on the differentially expressed proteins between NoTf accept and NoTf no accept cells. This revealed enrichment in BMP signaling, protein phosphorylation, and the p38 MAPK cascade (Fig. 4a), supporting a role for BMP in the early phenotypic shift of NoTf accept cells. Among these genes,

we selected six associated with BMP and/or p38 signaling and examined their expression in various sorted cell populations (illustrated in Fig. 3a). Interestingly, ID1 (a transcriptional regulator and BMP target gene), Nup214 (nucleoporin regulator of BMPR signaling cascade)[21] and spartin (an inhibitor of BMP signaling) were consistently up- or down-regulated in NoTf acceptor cells, to a level comparable to that observed in Tf cells, and solely in post-TNT transfer conditions (Fig. 4b). ATF2, positioned at the interface of both signaling pathways, was underexpressed in NoTf acceptor cells, at levels comparable to those in Tf cells. Lastly, Rac1 and Desmoglein-3, components of a complex involved in actin bundling and F-actin stabilization, and regulated by the p38 signaling cascade, were overexpressed in NoTf cells that had received material *via* TNTs (Fig. 4b).

As a key regulator of mammary cell transformation[15], the expression of BMPR1b increased with transformation and was localized within TNTs, particularly in bulges, in both normal primary and BMP2/IL6-transformed mammary cells (Fig. 4c). This was concomitant to the activation of both canonical p-SMAD1/5/8/SMAD1/5/8, and non-canonical p-p38/p38 and p-ERK/ERK cascades (Extended Data Fig.4a,b). Correlative light (scanning) electron microscopy (CLEM) enables to distinguish intra- from extra-cellular epitopes by overlaying optical and scanning electron images of the same region. Confocal imaging revealed a continuum of BMPR1b in cell bodies, as well as in or on TNTs. However, SEM did not reveal any extracellular BMPR1b epitopes at TNTs (Fig. 4d). This suggests an extracellular localization in the cell body and an intraluminal presence in TNTs, consistent with BMPR1b trafficking through/within TNTs. We then performed *BMPR1b* silencing in Tf cells, and although incomplete (Fig. 4e,f), this led to a marked reduction in the number of TNTs, and completely abolished the formation of long TNTs (Fig. 4g). Silencing of G protein-coupled estrogen receptor 1 (*GPER*) was used as a control, as no link between GPER and TNT formation or function has been reported to date. Despite being more efficient than *BMPR1b* silencing (Fig. 4f), *GPER* knockdown had no effect on TNT number or length (Fig. 4e,g). These

findings indicate that BMPR1b specifically contributes to the formation and elongation of TNTs, particularly of long ones.

To evaluate whether BMPR1b transfer via TNTs could sensitize NoTf cells to a BMP2/IL6-enriched microenvironment, the four cell populations sorted by flow cytometry (Figs. 3a, 4h) were analyzed for BMPR1b mRNA expression, which was found ~8-fold higher in NoTf accept cells previously connected *via* TNTs, compared to a ~2-fold increase when TNT formation was blocked using a Transwell™ method (Fig. 4i). This supports a role for TNT-mediated BMP pathway activation.

Collectively, these findings underscore the prominent activation of the BMP pathway, particularly through its non-canonical p38 signaling cascade, in NoTf cells acceptor of material from Tf cells, *via* TNT-mediated transfer. BMPR1b plays a dual role by promoting TNT formation and being transferred to acceptor cells, where it contributes to enhanced BMP signaling.

TNT-mediated delivery of BMPR1b sensitizes acceptor cells to a transforming microenvironment.

In order to assess the long-term impact of BMPR1b transfer, sorted cells were cultured for 14-16 weeks with or without BMP2/IL6, mimicking luminal breast tumor conditions (Fig. 4h). BMPR1b protein levels rose between weeks 6 and 10 before stabilizing, in NoTf accept cells exposed to BMP2/IL6 post-sorting (Fig. 5a left), reaching the highest expression among all populations by week 14 (Fig. 5a right; Extended Data Fig. 4c,d). Accordingly, both canonical (p-SMAD1/5/8/SMAD1/5/8) and non-canonical (p-p38/p38) signalings were activated upon 4 to 6 week-exposure to BMP2/IL6 in NoTf accept cells (Fig. 5b,c; Extended Data Fig. 4e,f). Surprisingly, the p38 cascade was strongly activated, as early as 4 weeks post sorting, with exposure to the cytokines.

To further investigate how material uptake *via* TNTs contributes to preneoplastic features in NoTf cells, we cross-referenced our proteomic and transcriptomic datasets[12] and identified three tumor-associated genes significantly upregulated during transformation: *HOXB6*[22], *CCND2*[23], and *EREG*[24] (Fig. 5d). Transcript levels of these genes were markedly increased in NoTf acceptor cells following an 8-day exposure to Tf cells with formation of TNT contacts, compared to NoTf controls (Fig. 5e), supporting the notion that TNT-mediated transfer promotes a shift towards a preneoplastic state. Though not significantly, the protein levels, HoxB6, Cyclin D2 and (pro)-epiregulin also tended to increase with transformation (Extended Data Fig. 5a). *HRAS* was also overexpressed in NoTf accept cells, though to a lesser extent than other genes, further substantiating a shift towards a preneoplastic status. However, *HRAS* was neither involved in TNT formation, nor in TNT-mediated rewiring of acceptor cells (Fig. 3f-i). As a negative control, we selected *UFM1*, a gene involved in endoplasmic reticulum stress, a cellular insult suggested to contribute to TNT development[25]. *UFM1* transcript levels remained unchanged regardless of transformation status or material uptake (Extended data Fig. 5b,c), indicating that although ER stress may be present, it is not a key driver of the cellular behavior described here.

NoTf acceptor cells grown in the presence of BMP2/IL6, up to 16 weeks post-TNT transfer and sorting (Fig. 5f,g), displayed anchorage-independent growth at earlier time points and with a number of clones obtained comparable to that of Tf cells (Fig. 5g; Extended Data Fig. 6a). Potential cross-contamination between Tf and NoTf sorted cell samples was ruled out based on the specific fluorescence of derived soft agar clones (Extended Data Fig. 6b). These features are hallmarks of a preneoplastic transformation, observed exclusively in cells that had established TNT contacts with transformed cells prior to sorting, enabling the transfer of transforming information. BMPR1b, trafficked via TNTs from Tf to NoTf cells, thus emerges as a key mediator of this process.

Hence, these findings highlight the central role of the BMP pathway in driving the preneoplastic switch in NoTf cells that received material from Tf cells, in close association with TNT-mediated

transfer. This intercellular communication primes non-transformed cells to respond to a tumor-promoting microenvironment, ultimately contributing to the propagation of transformation (Fig. 5h).

Discussion

Our findings reveal that TNT-mediated transfer of BMPR1b from transformed to non-transformed cells activates the BMP signaling pathway in acceptor cells, sensitizing them to a tumor-promoting microenvironment and initiating early features of transformation.

TNTs have already been shown to connect cells of various phenotypes, such as mammary epithelial transformed or metastatic cells with stromal cells[26]. Recently, TNTs were shown to enhance the metastatic capacity of cancer cells that receive mitochondria from neurons in primary tumors, shedding new light on how the nervous system supports cancer metabolism and metastatic dissemination[2]. Previous studies have extensively documented the transfer of cellular material, most notably mitochondria, from the tumor microenvironment, particularly stromal cells, to cancer cells. In contrast, the delivery of material from transformed cells to non-transformed neighbors, remains largely unexplored, especially at early stages of transformation. To our knowledge, our study is the first to investigate the functional impact of TNT-mediated material exchange between epithelial cells, on the predisposition of non-transformed cells to transformation (adopting a preneoplastic status). Our results reveal that TNTs play a role in the predisposition of non-transformed cells to tumoral transformation, by transferring information and modifying their sensitivity to a BMP2/IL6-enriched microenvironment. Although donor-to-acceptor material transfer through EVs and secretion of soluble compounds occurred, it remained low to negligible, indicating that the processes mainly relied on physical TNT-mediated cell/cell communications. We showed that this directional transfer from transformed to non-transformed cells (normal

primary or from cell lines), leads within days to the overexpression of tumor-related genes and of BMPR1b itself, evocative of a possible feedback loop that maintains transforming conditions (Fig. 5h). In this context, non-transformed cells undergo a metabolic rewiring, indicative of mitochondrial dysfunctions, and within weeks acquire phenotypic traits of preneoplasia, such as anchorage-independent growth, BMPR1b sustained overamplification and related mounting of a non-canonical signaling cascade. We then uncovered that the earliest events, within one week, comprised the overexpression of *HOXB6*, *CCND2* and *EREG* by non-transformed acceptor cells, after physical cell-to-cell contacts with transformed (donor) cells *via* TNTs. Interestingly, upregulation of these genes upon transformation has already been linked to other cancers, namely *HOXB6*, encoding a homeobox domain-containing transcription factor involved in development, is upregulated in acute myeloid leukemia, osteosarcoma, hepatocellular and colorectal carcinomas[22,27,28], with a possible role in cancer initiation[29]. *CCND2*, encoding cyclin D2, involved in DNA replication, cell division and cell cycle regulation, was reported to be dysregulated in gastric, thyroid and colorectal cancers[30], and its overexpression in breast cancer promotes MAPK-mediated cell proliferation and tumor growth[23,31]. Upregulation of *EREG,* encoding the secreted protein ligand of the EGF receptor (EGFR) epiregulin, is linked to breast cancer progression and resistance to tamoxifen by EGFR activation[24,32]. As expected, we observed an important mitochondrial trafficking within TNTs, likely contributing to metabolic rewiring of acceptor cells. Such rewiring has been documented to fuel ATP production, acceptor cell survival and proliferation, and sustain tumor growth and chemoresistance[33–36]. Moreover, the TNT-mediated unidirectional mitochondrial transfer from breast cancer-associated fibroblasts to cancer cells promotes OXPHOS and cancer cell invasiveness[37].

We reveal here a new biological function for BMP signaling in very early stages of breast cancer. We show that following TNT material transfer, including BMPR1b itself, *BMPR1B* becomes overexpressed in acceptor cells within a week. This further highlights the key role of this receptor

in early steps of mammary epithelial cell transformation[15]. Here, we detected the receptor within TNTs, overexpressed in transformed cells, and structurally contributing to TNT elongation. As BMP receptors are known to be located in lipid rafts, BMPR1b could induce TNT formation *via* its interaction with these microdomains[38], from which TNTs might arise[39,40]. These cholesterol-rich microdomains provide high curvature and elasticity necessary for membrane deformation linked to TNT formation. Cholesterol levels together with lipid rafts increase upon transformation, as previously evidenced in prostate and breast cancer cell lines[41], further substantiated by our proteomic data with acceptor cells displaying enhanced expression of EST1, a carboxylesterase hydrolyzing cholesterol esters into free cholesterol. Additionally, BMP2 was reported to promote actin polymerization via PI3Kα activation[42]. We herein observed that *LCP1* was upregulated upon transformation, concomitantly to its protein Plastin-2, in acceptor cells following TNT transfer. Plastin-2 is a key actin-bundling protein involved in the formation of cellular protrusions[43], and is overexpressed in epithelial-derived cancers including breast cancer[44]. Its overexpression has been associated with cancer cell migration, invasion, metastasis[45] and chemoresistance[46]. Plastin-2 activation depends on serine 5 phosphorylation *via* ERK/MAPK, PI3K, and PKA/PKC pathways, enabling its recruitment to actin filaments and promoting bundling and protrusion elongation, as shown in breast carcinoma[47]. This is consistent with findings from the Zurzolo's group, showing that TNT induction by Eps8 involves its actin-bundling activity[48]. Altogether, this might explain the higher number of TNTs observed upon transformation.

At the functional level, the analysis of acceptor cells sorted post-TNT transfer, revealed their gradual transformation over weeks, faster and more extensively than non-acceptor cells, concomitant to a progressive but sustained activation of BMP signaling. This activation induced an initial burst in p38 downstream response, observed only when TNTs mediated cellular contacts. Within days of TNT-mediated contact, acceptor cells overexpressed tumor-related genes such as *HOXB6, CCND2,* and *EREG*, as well as *BMPR1B* itself, suggesting a possible feedback loop that

sustains transforming conditions. Over the following weeks, these cells underwent mitochondrial dysfunction, metabolic rewiring, and exhibited preneoplastic traits, including BMPR1b overamplification and activation of a non-canonical signaling cascade. Importantly, experiments on TNT-forming capacities of mammary cell models, where transformation of either normal primary[20] or MCF10A cells[49] is « switched on » by the H-Ras oncoprotein, reported fewer and shorter TNTs connecting cells. *HRAS* is overexpressed in invasive breast tumors, and the prevalence of *HRAS* mutations in luminal types is negligible[50]. Therefore, although widely used, these mammary models do not mimic the *in vivo* BMP2-dependent and inflammatory context of non-invasive luminal breast tumors that our model recapitulates[13,15]. This further strengthens the link we uncovered between TNT induction, BMP signaling and the transfer of transforming information at early oncogenesis stages. Therefore, aberrant regulation of the BMP pathway appears as a crucial mechanism in early stages of cell transformation[14,15], with the establishment of an amplification loop. We unveiled that TNTs not only transfer mitochondria but, for the first time, a signaling receptor, BMPR1b. This transfer sensitizes acceptor cells to BMP2 signals of the microenvironment, triggering a cascade of molecular events that culminate in metabolic rewiring, phenotypic changes, and acquisition of anchorage-independent growth of previously non-transformed cells (Fig. 5h). Combined with the recent demonstration that TNTs are capable of transferring material *in vivo*[51], our work provides the foundation for a new concept: the propagation, through TNTs, of a preneoplastic state within a population of initially non-transformed mammary cells. This process could precede tumor development and identify BMPR1b as a major early contributor of the BMP-dependent preneoplastic switch of acceptor cells.

Data availability statement. The mass spectrometry proteomics data have been deposited to the ProteomeXchange Consortium via the PRIDE (https://www.ebi.ac.uk/pride/)[52,53] partner repository, with the dataset identifier PXD060023. Transcriptomic data have been deposited on the Gene Expression Omnibus repository, GSE186734[13].

Acknowledgements. We thank P. Battiston-Montagne, M. Gautier and C. Vanbelle (CRCL, platform PIC), and D. Ressnikoff (SFR Santé Lyon Est, CIQLE). We also thank C. Dalverny for expert assistance with CLEM (Centre Technologique des Microstructures CTμ), and F. Guillonneau, A. Boissard and C. Henry for expert assistance with proteomics. We thank the "AniRA lentivectors production facility" from the CELPHEDIA Infrastructure and SFR Biosciences, UAR3444/CNRS, US8/Inserm, ENS de Lyon, UCBL, especially G. Froment, D. Nègre and C. Costa. We thank J. Brocard, head of the LYMIC-PLATIM UAR 3444 / US8 microscopy platform (ENS Lyon, Univ Lyon 1). We thank B. Manship for english proofreading and Dr P. Mehlen for inspiring discussions. Some illustrations were created in https://BioRender.com.

This work was supported by Agence Nationale de la Recherche (VMS, ANR-10-LABX-0061, ANR-CESA-018-04 and Convergence PLAsCAN ANR-17-CONV-0002); Ligue Nationale contre le Cancer Dept Ain, Rhône (VMS) and Saône et Loire (EIP) ; Fondation ARC (VMS, SFI20111203500, PJA20171206331) ; the ERiCAN program of Fondation MSD-Avenir (VMS/EIP, DS-2018-0015) and Associations [Déchaîne Ton Cœur (VMS); Ruban Rose Prix Avenir 2021 (VMS) ; Comité féminin pour le dépistage du cancer du sein 74 (VMS) ; Symatese Fondation (VMS), and Fondation pour la Recherche Médicale (équipe FRM EQU202203014695 VMS).

Contributions: V.M.S. and E-I.P designed and supervised the study, conceived methodological developments and acquired funding. V.M.S. provided administrative support. C.C.M., S.L. and B.G. collaborated in study design, contributed to methodological developments and data interpretations. K.G. performed RNA-seq and proteomic bioinformatic data analyses, and statistical gene-expression analyses. C.C.M., T.T.N., A.B. and E-I.P. performed and interpreted the experiments. C.D. designed and performed SEM and CLEM microscopy experiments. F.G., A.B. and C.H. performed proteomic analyses, and F.G. interpreted proteomic data. E.D. provided primary breast samples, and assisted with their processing. V.M.S and E-I.P. wrote the manuscript. All authors reviewed the manuscript and approved the final version for publication.

References

1. Mao, X. *et al.* Crosstalk between cancer-associated fibroblasts and immune cells in the tumor microenvironment: new findings and future perspectives. *Mol. Cancer* **20**, 131 (2021).

2. Hoover, G. *et al.* Nerve-to-cancer transfer of mitochondria during cancer metastasis. *Nature* **644**, 252–262 (2025).

3. Bayik, D. & Lathia, J. D. Cancer stem cell-immune cell crosstalk in tumour progression. *Nat. Rev. Cancer* **21**, 526–536 (2021).

4. Ju, F. *et al.* Characteristics of the cancer stem cell niche and therapeutic strategies. *Stem Cell Res. Ther.* **13**, 233 (2022).

5. Duro, M. G., Tavares, L. A., Furtado, I. P., Saint-Pol, J. & D'Angelo, G. Protrusion-Derived Extracellular Vesicles (PD-EVs) and Their Diverse Origins: Key Players in Cellular Communication, Cancer Progression, and T Cell Modulation. *Biol. Cell* **117**, e70018 (2025).

6. Resnik, N., Erman, A., Veranič, P. & Kreft, M. E. Triple labelling of actin filaments, intermediate filaments and microtubules for broad application in cell biology: uncovering the cytoskeletal composition in tunneling nanotubes. *Histochem. Cell Biol.* **152**, 311–317 (2019).

7. Huang, P. *et al.* BMP-2 induces EMT and breast cancer stemness through Rb and CD44. *Cell Death Discov.* **3**, 17039 (2017).

8. Rustom, A., Saffrich, R., Markovic, I., Walther, P. & Gerdes, H.-H. Nanotubular highways for intercellular organelle transport. *Science* **303**, 1007–1010 (2004).

9. Pinto, G., Brou, C. & Zurzolo, C. Tunneling Nanotubes: The Fuel of Tumor Progression? *Trends Cancer* **6**, 874–888 (2020).

10. Vignais, M.-L., Caicedo, A., Brondello, J.-M. & Jorgensen, C. Cell Connections by Tunneling Nanotubes: Effects of Mitochondrial Trafficking on Target Cell Metabolism, Homeostasis, and Response to Therapy. *Stem Cells Int.* **2017**, 6917941 (2017).

11. Zhang, J.-Q. *et al.* In vitro and in vivo detection of tunneling nanotubes in normal and pathological osteoclastogenesis involving osteoclast fusion. *Lab. Investig. J. Tech. Methods Pathol.* **101**, 1571–1584 (2021).

12. Pinto, G. *et al.* Patient-derived glioblastoma stem cells transfer mitochondria through tunneling nanotubes in tumor organoids. *Biochem. J.* **478**, 21–39 (2021).

13. Guyot, B. *et al.* An Early Neoplasia Index (ENI10), Based on Molecular Identity of CD10 Cells and Associated Stemness Biomarkers, is a Predictor of Patient Outcome in Many Cancers. *Cancer Res. Commun.* **3**, 1966–1980 (2023).

14. Guyot, B., Lefort, S., Voeltzel, T., Pécheur, E.-I. & Maguer-Satta, V. Altered BMP2/4 Signaling in Stem Cells and Their Niche: Different Cancers but Similar Mechanisms, the Example of Myeloid Leukemia and Breast Cancer. *Front. Cell Dev. Biol.* **9**, 787989 (2021).

15. Chapellier, M. *et al.* Disequilibrium of BMP2 levels in the breast stem cell niche launches epithelial transformation by overamplifying BMPR1B cell response. *Stem Cell Rep.* **4**, 239–254 (2015).

16. Sharma, R. *et al.* BMP4 enhances anoikis resistance and chemoresistance of breast cancer cells through canonical BMP signaling. *J. Cell Commun. Signal.* **16**, 191–205 (2022).

17. Huang, L. *et al.* Revealing the structure and organization of intercellular tunneling nanotubes (TNTs) by STORM imaging. *Nanoscale Adv.* **4**, 4258–4262 (2022).

18. Sáenz-de-Santa-María, I., Henderson, J. M., Pepe, A. & Zurzolo, C. Identification and Characterization of Tunneling Nanotubes for Intercellular Trafficking. *Curr. Protoc.* **3**, e939 (2023).

19. Cordero Cervantes, D. & Zurzolo, C. Peering into tunneling nanotubes-The path forward. *EMBO J.* **40**, e105789 (2021).

20. Elenbaas, B. *et al.* Human breast cancer cells generated by oncogenic transformation of primary mammary epithelial cells. *Genes Dev.* **15**, 50–65 (2001).

21. Sapkota, G., Alarcón, C., Spagnoli, F. M., Brivanlou, A. H. & Massagué, J. Balancing BMP signaling through integrated inputs into the Smad1 linker. *Mol. Cell* **25**, 441–454 (2007).

22. Fischbach, N. A. *et al.* HOXB6 overexpression in murine bone marrow immortalizes a myelomonocytic precursor in vitro and causes hematopoietic stem cell expansion and acute myeloid leukemia in vivo. *Blood* **105**, 1456–1466 (2005).

23. Ouyang, J. *et al.* LncRNA PRNCR1 Promotes Breast Cancer Proliferation and Inhibits Apoptosis by Modulating microRNA-377/CCND2/MEK/MAPK Axis. *Arch. Med. Res.* **52**, 471–482 (2021).

24. He, M. *et al.* The miR-186-3p/EREG axis orchestrates tamoxifen resistance and aerobic glycolysis in breast cancer cells. *Oncogene* **38**, 5551–5565 (2019).

25. Wang, Y., Cui, J., Sun, X. & Zhang, Y. Tunneling-nanotube development in astrocytes depends on p53 activation. *Cell Death Differ.* **18**, 732–742 (2011).

26. Burtey, A. *et al.* Intercellular transfer of transferrin receptor by a contact-, Rab8-dependent mechanism involving tunneling nanotubes. *FASEB J. Off. Publ. Fed. Am. Soc. Exp. Biol.* **29**, 4695–4712 (2015).

27. Huang, H. *et al.* Hsa_circ_0007031 promotes the proliferation and migration of osteosarcoma cells by sponging miR-196a-5p to regulate the HOXB6. *Biochem. Pharmacol.* **214**, 115667 (2023).

28. Li, Y. & Jiang, A. ST8SIA6-AS1 promotes hepatocellular carcinoma by absorbing miR-5195-3p to regulate HOXB6. *Cancer Biol. Ther.* **21**, 647–655 (2020).

29. Vider, B. Z. *et al.* Deregulated expression of homeobox-containing genes, HOXB6, B8, C8, C9, and Cdx-1, in human colon cancer cell lines. *Biochem. Biophys. Res. Commun.* **272**, 513–518 (2000).

30. Ding, Z.-Y. *et al.* Prognostic role of cyclin D2/D3 in multiple human malignant neoplasms: A systematic review and meta-analysis. *Cancer Med.* **8**, 2717–2729 (2019).

31. Zhong, H. *et al.* LncRNA GACAT3 predicts poor prognosis and promotes cell proliferation in breast cancer through regulation of miR-497/CCND2. *Cancer Biomark. Sect. Dis. Markers* **22**, 787–797 (2018).

32. Abba, M. C. *et al.* LINC00885 a Novel Oncogenic Long Non-Coding RNA Associated with Early Stage Breast Cancer Progression. *Int. J. Mol. Sci.* **21**, 7407 (2020).

33. Hekmatshoar, Y., Nakhle, J., Galloni, M. & Vignais, M.-L. The role of metabolism and tunneling nanotube-mediated intercellular mitochondria exchange in cancer drug resistance. *Biochem. J.* **475**, 2305–2328 (2018).

34. Marlein, C. R. *et al.* CD38-Driven Mitochondrial Trafficking Promotes Bioenergetic Plasticity in Multiple Myeloma. *Cancer Res.* **79**, 2285–2297 (2019).

35. Nakhle, J. *et al.* Mitochondria Transfer from Mesenchymal Stem Cells Confers Chemoresistance to Glioblastoma Stem Cells through Metabolic Rewiring. *Cancer Res. Commun.* **3**, 1041–1056 (2023).

36. Watson, D. C. *et al.* GAP43-dependent mitochondria transfer from astrocytes enhances glioblastoma tumorigenicity. *Nat. Cancer* **4**, 648–664 (2023).

37. Goliwas, K. F. *et al.* Mitochondrial transfer from cancer-associated fibroblasts increases migration in aggressive breast cancer. *J. Cell Sci.* **136**, jcs260419 (2023).

38. Hirschhorn, T., Levi-Hofman, M., Danziger, O., Smorodinsky, N. I. & Ehrlich, M. Differential molecular regulation of processing and membrane expression of Type-I BMP receptors: implications for signaling. *Cell. Mol. Life Sci. CMLS* **74**, 2645–2662 (2017).

39. Reindl, J., Shevtsov, M., Dollinger, G., Stangl, S. & Multhoff, G. Membrane Hsp70-supported cell-to-cell connections via tunneling nanotubes revealed by live-cell STED nanoscopy. *Cell Stress Chaperones* **24**, 213–221 (2019).

40. Thayanithy, V. *et al.* Tumor exosomes induce tunneling nanotubes in lipid raft-enriched regions of human mesothelioma cells. *Exp. Cell Res.* **323**, 178–188 (2014).

41. Li, Y. C., Park, M. J., Ye, S.-K., Kim, C.-W. & Kim, Y.-N. Elevated levels of cholesterol-rich lipid rafts in cancer cells are correlated with apoptosis sensitivity induced by cholesterol-depleting agents. *Am. J. Pathol.* **168**, 1107–1118; quiz 1404–1405 (2006).

42. Gamell, C. *et al.* BMP2 induction of actin cytoskeleton reorganization and cell migration requires PI3-kinase and Cdc42 activity. *J. Cell Sci.* **121**, 3960–3970 (2008).

43. Ishida, H., Jensen, K. V., Woodman, A. G., Hyndman, M. E. & Vogel, H. J. The Calcium-Dependent Switch Helix of L-Plastin Regulates Actin Bundling. *Sci. Rep.* **7**, 40662 (2017).

44. Lin, C. S., Park, T., Chen, Z. P. & Leavitt, J. Human plastin genes. Comparative gene structure, chromosome location, and differential expression in normal and neoplastic cells. *J. Biol. Chem.* **268**, 2781–2792 (1993).

45. Riplinger, S. M. *et al.* Metastasis of prostate cancer and melanoma cells in a preclinical in vivo mouse model is enhanced by L-plastin expression and phosphorylation. *Mol. Cancer* **13**, 10 (2014).

46. Janji, B. *et al.* The actin filament cross-linker L-plastin confers resistance to TNF-alpha in MCF-7 breast cancer cells in a phosphorylation-dependent manner. *J. Cell. Mol. Med.* **14**, 1264–1275 (2010).

47. Machado, R. A. C. *et al.* L-plastin Ser5 phosphorylation is modulated by the PI3K/SGK pathway and promotes breast cancer cell invasiveness. *Cell Commun. Signal. CCS* **19**, 22 (2021).

48. Delage, E. *et al.* Differential identity of Filopodia and Tunneling Nanotubes revealed by the opposite functions of actin regulatory complexes. *Sci. Rep.* **6**, 39632 (2016).

49. Dawson, P. J., Wolman, S. R., Tait, L., Heppner, G. H. & Miller, F. R. MCF10AT: a model for the evolution of cancer from proliferative breast disease. *Am. J. Pathol.* **148**, 313–319 (1996).

50. Kim, S.-J. *et al.* Cooperation between oncogenic NRF2 and wild-type HRAS promotes progression of breast cancer. *Cell. Signal.* **134**, 111920 (2025).

51. Korenkova, O. *et al.* Tunneling nanotubes enable intercellular transfer in zebrafish embryos. *Dev. Cell* **60**, 524-534.e3 (2025).

52. Perez-Riverol, Y. *et al.* PRIDE Inspector Toolsuite: Moving Toward a Universal Visualization Tool for Proteomics Data Standard Formats and Quality Assessment of ProteomeXchange Datasets. *Mol.*

Cell. Proteomics MCP **15**, 305–317 (2016).

53. Perez-Riverol, Y. *et al.* The PRIDE database at 20 years: 2025 update. *Nucleic Acids Res.* **53**, D543–D553 (2025).

Figure Legends.

Fig. 1 | Structural characterization of TNTs upon mammary cell transformation. a, Schematic of our MCF10A-derived cell lines[13]. b, Immunofluorescence images of actin (red) in TNTs, observed by Airyscan confocal microscopy with 40x oil objective. Nuclei, Hoechst labeling (blue). Scale bars, 20 μm. c, TNT number (> 8 μm) quantification *per* 100 cells (left, n = 9 biological replicates), and % of long TNTs (> 50 μm; right, n = 4 biological replicates). Ten Z-stacks of 10 sections each were taken *per* condition, and 100 cells minimum *per* experiment were counted. TNTs were counted and measured in each Z-stack. Error bars depict SD. P-values were calculated with one-way ANOVA with post-hoc Tukey test (ns, not significant; * $p < 0.05$; ** $p < 0.01$; *** $p < 0.001$). d, SEM images of TNTs of MCF10A-CT, MC26 and M1B26 cells. Black arrow, TNT bulge. Scale bars MCF10A-CT: 40 and 50 μm; MC26: 50 and 5 μm; M1B26: from left to right: 20, 3, 20, 3 μm. e, TEM images of an open-ended TNT linking two M1B26 cells, with mitochondria (red asterisks). Scale bars, 5 μm (low mag), 500 nm (high mag). f, Immunofluorescence images of mitochondria (green) in MCF10A-CT and M1B26 cells. Actin, red; nuclei, blue. Scale bars, 20 μm. g, Immunofluorescence images of actin (red) in mammary acini grown from MC26 and M1B26 cells. Scale bars, 5 μm. Right, 3D-projection of a TNT linking two M1B26 cells, obtained with Zeiss ZENlite3.6 software. Actin, red; nuclei, blue. h, Images of TNTs linking M1B26 (GFP, green, and transmitted light) to normal human primary mammary fibroblasts (transmitted light). Nuclei, blue. Scale bars, 20 μm. i, Images of TNTs linking M1B26 (GFP, green) to normal human primary mammary cells. Actin, red; nuclei, blue. Asterisks: emerging from M1B26 (green); between both cell types (red). Scale bars: top, 20 μm, bottom, 10 μm.

Fig. 2 | TNTs link transformed and non-transformed mammary cells, favoring a directional transfer of information. a, Fluorescence images of GFP-labeled-M1B26 (transformed - Tf; green) and mCherry-labeled MCF10A (non-transformed - NoTf; red) cells, after 48 h in coculture. Scale bars, 5 µm. b,c, Relative number of TNTs linking NoTf to Tf, or Tf to NoTf cells (b) and TNT ratio defined as $\frac{NoTf>Tf}{NoTf-NoTf}$ (black arrows *vs* red lines) or $\frac{Tf>NoTf}{Tf-Tf}$ (black arrows *vs* green lines) after 48 h in coculture (c). Z stacks of 10 sections each were taken *per* condition and 100 cells minimum were counted. TNTs were counted and measured in each Z-stack. Error bars depict SD. Statistical significance was calculated using an unpaired Student's two-sided t test with Welch's correction (n = 5 biological replicates; *** $p < 0.001$). d, Fluorescence images of material transfer (green dots) from Tf (green) to NoTf cells. Membranes, red; nuclei, blue. Scale bars: 100 µm, in zoom 20 µm. e, Time-lapse snapshots of green material trafficking within a TNT bulge (*), from a (green) Tf to NoTf cells after 48 h in coculture. Membranes, red; nuclei, blue. Scale bar, 100 µm; images recorded for 75 min, with one image every 18 min (see Supplementary Movie 1). f, Flow cytometry analysis of an 8-day coculture of green Tf and red NoTf cells (f), with a schematic of NoTf accepting material from Tf cells (top: NoTf accept green, red cell with green dots), and Tf cells accepting material from NoTf cells (bottom: Tf accept red, green cell with red dots). g,h, Quantification of the percentage of exchange (g; n = 8 biological replicates) and fluorescence intensity (h; n = 7 biological replicates), for indicated transfer. Error bars depict SD. Statistical significance was calculated using an unpaired Student's two-sided t test with Welch's correction (*** $p < 0.001$). i, Schematic of the experimental design of coculture experiments. j,k, Quantification of the number of acceptor cells *per* 10,000 cells (j), and fluorescence intensity (k), in standard or Transwell™ cocultures, for indicated transfer involving normal human primary mammary (normal) and M1B26 cells (Tf). Error bars depict SD. Statistical significance was

calculated using an unpaired Student's two-sided t test with Welch's correction (n = 3 biological replicates; ns, not significant; * $p < 0.05$; ** $p < 0.01$).

Fig. 3 | TNT-dependent phenotypic changes of non-transformed cells acceptor of material from transformed cells. a, Schematic of the experimental design: 4 cell populations, sorted by flow cytometry (NoTf, Tf, NoTf in coculture without fluorescent transfer [non-transformed non-acceptor cells - NoTf no accept], NoTf in coculture with fluorescent transfer [non-transformed acceptor cells - NoTf accept]), underwent proteomic analyses and RT-qPCR. b-c, Volcano plot (b) showing log2 enrichment of individual proteins in NoTf accept compared to NoTf no accept cells. P-value threshold was set at 0.05 and 0.8 for Log_2 fold change. To obtain a larger pool of hits, it was lowered to 0.5, generating a list of 193 proteins upregulated in NoTf accept cells, used to generate the GOBP subset with STRING (https://string-db.org; c). d,e Box and whiskers plots of Log_2LFQ values (Protein Levels) of EST1 (*CES1*), Plastin-2 (*LCP1*), Rab-6B (*RAB6B*), TRIQK (*TRIQK*) (d), and H-Ras and K-Ras (e), for indicated sorted cell populations. Statistical significance was calculated using one-way ANOVA with post-hoc Tukey test (n = 5 biological replicates; * $p < 0.05$; ** $p < 0.01$; *** $p < 0.001$; **** $p < 0.0001$). For clarity, comparisons with Tf cells were omitted. f,g Immunofluorescence images of actin (red) and tubulin (green) in (f) HMLE and HMLER cells, and (g) MCF10A, MCF10.AT1 and MCF10.DCIS cells. Nuclei, blue. Scale bars = 20 μm. h,i, From left to right: quantification of TNT number *per* cell, average length, and percentage of long TNTs in indicated cell lines. Ten Z-stacks of 10 sections each were taken *per* condition and 100 cells minimum *per* experiment were counted. TNTs were counted and measured in each Z-stack. Statistical significance was calculated using an unpaired Student's two-sided t test with Welch's correction (n = 8 and n = 5 biological replicates for HMEC-derived and MCF10A-derived cell lines, respectively; ns, not significant; ** $p < 0.01$).

Fig. 4 | Actors of the BMP signaling pathway are transferred to acceptor cells through TNTs. a, GOBP subset from a list of 6 protein hits dysregulated between NoTf accept and NoTf no accept cells, generated through STRING from proteins of the BMP and p38 pathways, chosen from the literature. The size of each circle represents the number of genes in the respective category; the intensity of the color represents the P-value, determined by a hypergeometric test. b, Box and whiskers plots of Log_2LFQ values (Protein Levels) of ID1 (*ID1*), Nup214 (*NUP214*), Spartin (*SPART*), ATF2 (*ATF2*), Rac1 (*RAC1*) and desmoglein-3 (*DSG3*), for indicated sorted cell populations. Statistical significance was calculated using one-way ANOVA with Dunnett's multiple comparison test (n = 5 biological replicates; * $p < 0.05$; ** $p < 0.01$; *** $p < 0.001$; **** $p < 0.0001$). For clarity, only comparison between NoTf and NoTf accept cells is shown. c, Immunofluorescence images of actin (red) and BMPR1b (green) in indicated cells. Nuclei (blue). Scale bars, 20 µm. d, Correlative light scanning electron microscopy (SEM) of BMPR1b, immunostained with Alexa Fluor®488-Fluoronanogold™ (green) in M1B26 cells. From left to right: confocal, SEM, zooms, correlative (overlay). Scale bars, 10 µm, unless otherwise indicated. e, Immunofluorescence of actin (green), after transfection with siRNA pools targeting *BMPR1b* (siBMPR1b) or *GPER* (siGPER). Non-targeting siRNA: siCTRL. f,g, *BMPR1B* and *GPER* transcript (f) and protein expression upon their silencing (f),with siCTRL set at 1 (n=4), and TNT number (> 8 µm) *per* cell and % of long TNTs (> 50 µm) upon indicated silencing, normalized against siCTRL (g). Error bars depict SD. Statistical significance was calculated using a Student's two-sided t test with Welch's correction (n = 4 biological replicates, *** $p < 0.001$). h, Schematic of experimental design: after sorting, cell populations were either lysed and subjected to RT-qPCR for selected transcript analyses, or grown for several weeks with or without BMP2/IL6, and immunoblot analyses performed at end points. i, RT-qPCR measurement of BMPR1b mRNA in indicated cell populations, the expression in NoTf cells set at 1. Statistical significance was

calculated using one-way ANOVA with post-hoc Tukey test (n = 5 biological replicates). For clarity, only comparison between NoTf accept and NoTf cells is shown (**** $p < 0.0001$).

Fig. 5 | Non-transformed cells acceptor of information *via* TNTs from transformed cells display preneoplastic features. a, Left, quantification of BMPR1b immunoblots performed on NoTf accept cells grown in the presence of BMP2/IL6, for indicated weeks post sorting. Box and whiskers plot of 6 biological replicates. Statistical significance was calculated using a one-way ANOVA with non-parametric Kruskal-Wallis test, and for clarity, only p-values ≤ 0.05 are indicated. Right, quantification of BMPR1b immunoblots performed on indicated cells, 14 weeks post sorting, with NoTf conditions set at 1 (n = 6 biological replicates). Statistical significance was calculated using a one-way ANOVA with post-hoc Tukey test (*** $p < 0.001$). b,c, Quantification of p-SMAD1/5/8/SMAD1/5/8 (b) and p-p38/p38 (c) immunoblots performed on NoTf accept cells grown in the presence of BMP2/IL6, for indicated weeks post sorting. Box and whiskers plot of 6 biological replicates. Statistical significance was calculated using a one-way ANOVA with non-parametric Kruskal-Wallis test, and for clarity, only p-values ≤ 0.05 are indicated. d, RNA-sequencing results of transcriptomic expression levels of *HOXB6, CCND2, EREG* and *HRAS* in indicated cell lines (n = 3 biological replicates). Data deposited on the Gene Expression Omnibus repository, GSE186734[13]. Error bars depict SD. Statistical significance was calculated using a one-way ANOVA with post-hoc Tukey test (* $p < 0.05$; ** $p < 0.01$; *** $p < 0.001$; **** $p < 0.0001$). e, RT-qPCR measurements of HOXB6, CCND2, EREG and HRAS mRNA in indicated cell populations, with the expression in NoTf cells set at to 1. Error bars depict SD. Statistical significance was calculated using a one-way ANOVA with post-hoc Tukey test (Biological replicates: n = 8 for HOXB6, n = 5 for CCND2, n = 7 for EREG, n = 8 for HRAS). For clarity, only comparison between NoTf accept and NoTf cells is shown (* $p < 0.05$; ** $p < 0.01$; *** $p < 0.001$; **** $p < 0.0001$). f, Schematic of long-term soft agar colony formation assays. g,

Quantification of soft agar clones of indicated sorted cells, after 16 weeks in culture with or without BMP2/IL6 (n = 3 biological replicates). Error bars represent SD. Statistical significance was calculated using a one-way Welch and Brown-Forsythe ANOVA test (* $p < 0.05$; ** $p < 0.01$; *** $p < 0.001$; **** $p < 0.0001$). For clarity, only p-values ≤ 0.05 are indicated, and comparisons with Tf cells are omitted. h, Model depicting how TNTs are involved in the propagation of a BMP-dependent preneoplastic state. Fibrils and fibers depict extracellular matrix components.

Materials & Methods.

Cell lines. MCF10A cells were purchased from ATCC (ATCC Batch#7635052). The MC26 cell line was obtained upon MCF10A chronic exposure to BMP2 and IL6, while M1B26 came from MCF10A first sorted on BMPR1b overexpression, then chronically exposed to BMP2 and IL6, and derived from a soft agar colony[13]. MCF10A, MCF10A.DCIS, MC26 and M1B26 were cultured in phenol-red free Dulbecco's Modified Eagle Medium Ham's F12 (DMEM-F12, Gibco), supplemented with 2% horse serum (Gibco), 10,000 U/ml - penicillin and 10,000 µg/ml - streptomycin (Gibco) (P/S), 10 µg/ml insulin (NovoRapid CLB pharmacy), 0.5 µg/ml hydrocortisone (Sigma), 100 ng/ml cholera toxin (Sigma), 20 ng/ml epithelial growth factor (Sigma). MCF10A.AT1 and MCF10A.DCIS, obtained from ATCC, were cultured with the same medium supplemented with 5% horse serum. MC26 and M1B26 culture medium was supplemented with 5 ng/ml BMP2 (R&D) and 10 ng/ml IL6 (Peprotech). HMEC cells were obtained from R. Weinberg's group (MIT, Massachussetts, USA). Cells were grown in 1:1 MEGM Complete Medium [Lonza/Clonetics, CC-3150] plus DMEM/F12 (1:1) with supplements : 10 ng/ml hEGF, 0.5 µg/ml hydrocortisone, 10 µg/ml insulin, 10,000 U/ml - penicillin and 10,000 µg/ml - streptomycin (Gibco). Cells were passed twice a week at 70% of confluence. Cells washed twice with Phosphate Buffer Saline (PBS, Life Technologies) were treated with 0.48 mM Versene (ThermoFischer, #15040066) for 20 min, or with trypsin 0.05% for 10 min at 37°C. After collecting

cells, neutralization was achieved with PBS/20% FBS. Plated cells were incubated at 37°C under 5% atmospheric CO_2.

Fluorescent cell lines generation. Fluorescent cells were obtained by viral transduction of parental ones with lentivirus produced in 293T cells by transfection of three plasmids encoding respectively for the viral envelope G of VSV (vesicular stomatitis virus), the structural and enzymatic proteins Gag and Pol of the lentivirus, and for a reporter gene mCherry or GFP (in collaboration with AniRA lentivectors production facility from the CELPHEDIA Infrastructure and SFR Biosciences, UAR3444/CNRS, US8/Inserm, ENS de Lyon / UCBL). Of note, these viruses are defective, meaning that no viral protein or particle are produced by cells after transduction.

Coculture of MCF10A and M1B26 cells. Cells were cocultured at a 50% ratio for up to 8 days in MCF10A complete medium. Fresh medium was added every 3-4 days. For the conditioned medium assay, the M1B26 green or MCF10A green supernatant was collected, centrifuged for 5 min at 800xg, and filtered on a 20µm-pore filter. Monocultures of fluorescent cells were grown for 8 days in this medium, and fresh one was added after 3-4 days. For cocultures in the Transwell system, a Transwell system with pores of 0.4 µm was used (Merck Millipore, #PHP01250). Four and ½ ml of MCF10A complete medium was added at the bottom, and 450 µl of MCF10A complete medium at the top of the insert. Cells were cocultured in the Transwell system for 8 days, and fresh complete medium was added after 3-4 days.

Gene silencing with siRNA. Silencing of BMPR1b and GPER was performed using small interfering RNAs, purchased at Horizon Discovery (ON-TARGETplus siRNA, SMARTpool siRNA). Cells were transfected through electroporation by a Neon Electroporator Device.

Western-Blotting. Cells were harvested, pelleted, and lysed in CHAPS buffer (40 mM Hepes pH 7.4, 120 mM NaCl, 2 mM EDTA, 0.3% CHAPS) and protease/phosphatase inhibitors (Roche Complete inhibitor cocktail #4693132001). Proteins were then assayed by spectrophotometry, along with a BSA standard curve, using the Pierce™ Coomassie Protein Assay Kit (Thermo Fisher Scientific). Twenty to 30 µg of proteins were used and mixed with 1X Laëmmli and H_2O, and samples boiled for 5 min at 95°C. The mixture was loaded onto 10% acrylamide gels, and run in 25 mM Tris, 192 mM glycine, 0.1% SDS. After transfer onto PVDF membranes previously activated in ethanol and transfer buffer (Biorad™ Transfer buffer, 20 % ethanol) using the Transblot Turbo™ from BioRad. Membranes were then incubated for 1h with TBST [Tris-buffered saline 1X (Euromedex) containing 0.1% Tween-20] with 5% fat-free BSA for membrane saturation at room temperature. Primary antibodies were incubated at 4°C overnight. Primary antibodies used were directed against BMPR1b (1:300 Abcam, ab78417 and 1:300 Santa Cruz, sc-515886), GAPDH (1:10,000 Cell Signaling Technology, #8884 and 1:50,000, Proteintech #600004-1), p-SMAD1/5/8 (1:500, Cell signalling, #13820), Smad1/5/8 (1:500, Santa Cruz, sc-6031-R), p-ERK (1:2,000, Cell Signalling Technology, #4370S), ERK (1:1,500, Cell Signalling Technology #4695S), p-p38 (1:2,000, BD Bioscience #612288), p38 (1:2,000, BD Biosciences, #612168), GPER (1:500 Novus Biologicals, #NLS4290 or 1:500, Invitrogen, #PA5-28647), EREG (1:400, abcam, #1041688-1), Cyclin-D2 (1:3,000, Proteintech, # 67048-i-IG), or HoxB6 (1:1,500, Santa Cruz, sc-166950), in 5% BSA. After TBST buffer washes, membranes were incubated at room temperature for 1h with horseradish peroxydase (HRP)-conjugated secondary antibodies goat anti-rabbit, goat anti-mouse or rabbit anti-goat secondary antibodies (Jackson, #111-035-003, #115-035-003, #305-035-003) at 1:10,000 in TBST/3% BSA. After extensive washings with TBST buffer, revelation was achieved through Clarity™ Western ECL Substrate (Biorad) and

Chemidoc™ Imaging System (Biorad). Protein bands were quantified using the ImageLab™ software.

Immunofluorescence. Cells were seeded on coverslips and grown at 60% of confluence. For staining BMPR1b and actin staining, the following protocol was used : after washing with PBS, fixation was performed for 20 min in 4% final paraformaldehyde (PFA) at room temperature (RT). After PBS washing, permeabilization and saturation were performed for 45 min with PBS/3% BSA/0.3% Triton X-100 at RT. After PBS washing, primary antibody against BMPR1b (1:300 #sc-293428 Santa Cruz) and its corresponding isotype were incubated overnight at 4°C. Coverslips were washed three times with PBS/3% BSA/0.1% Tween-20 for 10 min. Secondary antibody goat anti-mouse Dylight 488 diluted 1:1,000 was incubated for 45 minutes at RT, with 1:50,000 of Hoechst 33342 (Invitrogen #H3570) and Phalloidin AlexaFluor-Plus 647 (Invitrogen, #A30107). Then, cells were washed twice with PBS/3% BSA/0.1% Tween-20 for 5 minutes and twice with PBS for 5 minutes. Coverslips were then mounted using the Dako mounting medium (Agilent, ref S3023). For mitochondria staining, MitoTracker™ deep red or green were used (Thermofischer, #M22426 or #M7514, respectively). Microscopic observations were performed using the x40 oil immersion objective of a confocal Zeiss LSM980 microscope, with Airyscan mode. This was done at the LYMIC-PLATIM, Imaging and Microscopy Core Facility of SFR Biosciences (UMS3444), Lyon, France. Images were taken in 16-bit, and formatted via the Fiji software. For immunofluorescence staining of actin (Phalloidin) and tubulin, the following protocol optimized by the Dr. C. Zurzolo's team was used to identify and characterize TNTs[18]. Subconfluent cells were fixed for 15min at RT, with a 4% PFA/0.05% glutaraldehyde mixture in PBS. The fixation buffer was removed, and and cells incubated with 100 mM NH_4Cl for 10min at RT to quench the PFA-related autofluorescence. After PBS washing, cells were saturated with 2% BSA for 20 min at RT. The primary antibody against tubulin was diluted at 1:500 (Abcam #ab6046) in 2% BSA, and

incubated for 1h at RT, or OVN at 4°C. After PBS washing, cells were incubated with a secondary goat anti-rabbit antibody-488nm, diluted at 1:1,000 in 2% BSA, and incubated for 40 min in the dark at RT. After PBS washing, cells were finally incubated with phalloidin AlexaFluor Plus-647 (Invitrogen, #A30107) diluted at 1:1,000, and with Hoechst 33342 (Invitrogen, #H3570), diluted at 1:50,000 in 1% BSA, for 30 min in the dark. After PBS washing, slides were mounted using the Dako mounting medium (Agilent, S3023). Microscopic observations were performed with the objective 40x oil of a confocal Zeiss LSM980 microscope, with Airyscan mode. This was performed at the LYMIC-PLATIM, Imaging and Microscopy Core Facility of SFR Biosciences (UMS3444), Lyon, France, and at the imaging quantitative center of Lyon Est (CIQLE). Images were taken in 16-bit, and formatted *via* the Fiji software. TNTs were finally manually counted with the Fiji software.

Live imaging. Live imaging was performed after 48h of coculture in µslide 8-well plate with thin glass bottom (Ibidi, #80827), adequate for imaging. After PBS washing, cells were stained with Cell Mask deep red (at 1:500, #C10046, Invitrogen) and Hoechst (Invitrogen, #H3570, 1:500), diluted in complete medium, for 10 min at 37ºC. After PBS washing, complete fresh medium was added. Observations were performed using the Opera Phenix HCS microscope with the 40x water immersion objective.

RT-qPCR. For RT-qPCR analyses, pelleted cells were resuspended with 300µl Trizol reagent (Life Technologies™). Total RNA purification was achieved using direct-zol RNA MicroPrep w/ Zymo-Spin IC Columns extraction kit (Ozyme). For sorted fluorescent cells after coculture, RNA extraction was performed using the AllPrep DNA/RNA Micro Kit (Qiagen, #80284). C-DNA was then obtained using PrimeScript™ RT Reagent Kit (Takara kit), and qPCR then performed using

the SyberGreen Premix Ex Taq™ (Takara kit) as the fluorescent DNA intercalant, and amplicons read by a Light Cycle 480 (Roche, LC480). Results were normalized to housekeeping genes : TATA-binding protein (*TBP*) and hypoxanthineguanine phosphoribosyl transferase (*HPRT*) (see Table S3 for primers used). An additional normalization to control cells (MCF10A or MCF10A-CT) was also performed.

Proteomic analyses. *Sample preparation for proteome analysis*. Proteome analyses were performed at the Prot'ICO proteomics facility: FACS-sorted samples (FACS-Melody) were quickly thawed and proteins equivalent to 66,000 cells were concomitantly extracted and denatured while thiol groups were chemically reduced in 46 µl 5% SDS, containing 5 mM TCEP, 10 mM chloroacetamide, heated in a thermostatic shaker set at 95°C under 500xg for 30 min. Sonication was performed twice 30s using an ultrasonic sonicator bath (ThermoFisher Scientific). S-Trap Micro Spin Column was used according to the manufacturer's protocol (Protifi, Farmingdale, NY, USA), to trap precipitated proteins under acidic and hydrophobic conditions to remove detergents, and 1µg of porcine trypsin (Sciex) was used at 37°C overnight to cleave peptide bonds at carbonyl-side of lysine and arginine to generate bottom-up LC MS-compatible peptides. Resulting peptides were then cleared from potential insoluble material by centrifugation. Peptides were then speed-vacuum dried and resuspended in 0.1% formic acid (FA) before injection in LC-MS/MS with DIA-PASEF mode using a TIMS-TOF Pro 2 mass spectrometer (Bruker, Bremen, Germany).

LC-MS/MS setup. Each sample was loaded and separated on a C18 reverse phase column (Aurora Ultimate series 1.7µm particles size, 75µm inner diameter and 25cm length, IonOptics, Fitzroy, Australia) using a NanoElute 2 LC system with Hystar 6.3.1.8 software (Bruker, Bremen, Germany). Eluates were electrosprayed for a 60min-long duration of the hydrophobicity gradient ranging from 99% of solvent A containing 0.1% FA in milliQ-grade H_2O, to 27% of solvent B

containing 80% acetonitrile containing 0.1% FA in mQ-H_2O. The mass spectrometer acquired data throughout the elution process and operated in data-independent analysis (DIA) with PASEF-enabled method, using the TIMS-Control software v.5.1.8 (Bruker). Samples were injected in batch replicates in order to circumvent possible interferences of technical biases. The m/z acquisition range was 250–1201 with an ion mobility range of 0.7–1.25 1/*K*0 [V s/cm^2], which corresponded to an estimated cycle time of one second. DIA-PASEF windows, and collision energy were also left to default with a base of 0.85 1/*K*0 [V s/cm^2] set at 20 eV and 1.30 1/*K*0 [V s/cm^2] set at 59 eV. TOF mass calibration and TIMS ion mobility 1/*K*0 were performed linearly using three reference ions at 622, 922, and 1,222 m/z (Agilent Technology, Santa Clara, CA, USA)

LC-MS/MS raw data analysis. The raw data were extracted, normalized and analyzed using Spectronaut® 19.0.24 (Biognosys A.G. Schlieren, Switzerland) in DirectDIA+ mode, which modelized elution behavior, mobility and MS/MS events based on the "Uniprot/SwissprotKB model organism_9606_2024_04_03" FASTA sequence database of 45,514 human proteins and 381 entries of common contaminant proteins. Protein identification false discovery rate (FDR) was restricted to 1% maximum, and inter-injection data normalization. The enzyme's cleavage specificity was trypsin's. The precursor and fragment mass tolerances were set to default. Acetyl (protein N-term) and oxidation of methionines were set as variable modifications, while thiol groups from cysteines were considered completely alkylated by carbamidomethylation. A minimum of two ratios of peptides was required for relative quantification between groups. Protein quantification analysis was performed using Label-Free Quantification (LFQ) intensities. Spectronaut also linked Gene Ontology terms to identified protein using the EBI GO database, and its statistical tools were used to visualize data, assess reproducibility and quality to allow quantitative dataset comparisons. The mass spectrometry proteomics data have been deposited to the ProteomeXchange Consortium via the PRIDE[52,53] partner repository with the dataset identifier PXD060023.

Flow cytometry and cell sorting. After cell detachment as previously described, cells were resuspended in PBS/1% FBS. Sorting of cocultured cells was performed using the BD FACSMelody™ Cell Sorter. at the CRCL Flow cytometry platform, SFR Lyon-EST (CYLE). Results were analyzed with the FlowJo™ software.

Soft agar colony formation assay. Each well was coated with agarose 1.5% mixed with 2X complete medium. After polymerisation at RT, a top layer was added, containing agarose 0.9%, mixed with 2X complete medium containing 13,000 cells. PBS was added between wells, so that the agar would not dry out. Clone counting was performed manually after 3-4 weeks.

Electron microscopies. *Transmission EM.* Cell samples in Petri dishes were washed 3 times 15min in sodium cacodylate buffer 0.2M pH 7.3, and fixed for 1h in glutaraldehyde 2% in the same buffer at 0.1M. After washing in buffer, samples were prepared for TEM observations after Epoxy resin embedding and microtome ultrathin sectioning at the Center for Microstructure Technology (CTμ, Univ Lyon 1). Observations were performed with a Jeol 1400 Flash microscope operated at 200 kV, and equipped with a Gatan Rio 16 digital camera.

Correlative light scanning electron microscopy (CLEM). CLEM was performed in collaboration with the Center for Microstructure Technology (CTμ, Univ Lyon 1). Cells were plated on standard square coverslips ITO (22x22mm), and fixed with PFA 4% 20 min. After three washes with phosphate buffer 0.2M pH 7.2 for 20min, saturation was achieved using phosphate buffer with 3% BSA and 0.3% Triton X-100 for 45min. Incubation with primary antibodies and washings were performed as mentioned in the section “Immunofluorescence”. AlexaFluor-488 Fluoronanogold (FluoroNanogold™, Nanoprobes, #7201) was diluted at 1:100 in phosphate buffer with 1% BSA and 0.2% Tween-20, and incubated for 1h at RT. After washings, coverslips were mounted on a

"Shuttle and Find" Zeiss device, and the observation was done with a Zeiss confocal LSM800 microscope. After confocal observation, coverslips were washed three times with H_2O. Then silver enhancement was performed, using the HQ silver enhancement kit (Nanoprobes, #2012) for 5 minutes. After H_2O washings, cells were incubated with 1% final OsO4 in PBS 0.1M pH 7.2, for 45min. After H_2O washings, cells were incubated overnight with 20% acetone in H_2O. The following day, 100% acetone was added for 1h, followed by critical point drying for 2h. SEM imaging was then performed at the Center for Microstructure Technology (CTμ, Univ Lyon 1), using a scanning electron microscope Zeiss Merlin Compact VP.

Statistical methods: Normality test was performed using Shapiro-Wilk test. Mean comparisons of two samples were performed with an unpaired two-sided Student's t-test with Welch's correction. One-way Anova with post-hoc Tukey test, or with non-parametric Kruskal Wallis test, or a one-way Welch and Brown-Forsythe ANOVA were used, when multiple comparisons were performed. Statistical analyses were performed using GraphPad Prism software (La Jolla, CA). Significant p values are indicated by asterisks in the figures (* $p<0.05$; ** $p<0.01$; *** $p<0.001$, **** $p<0.0001$).

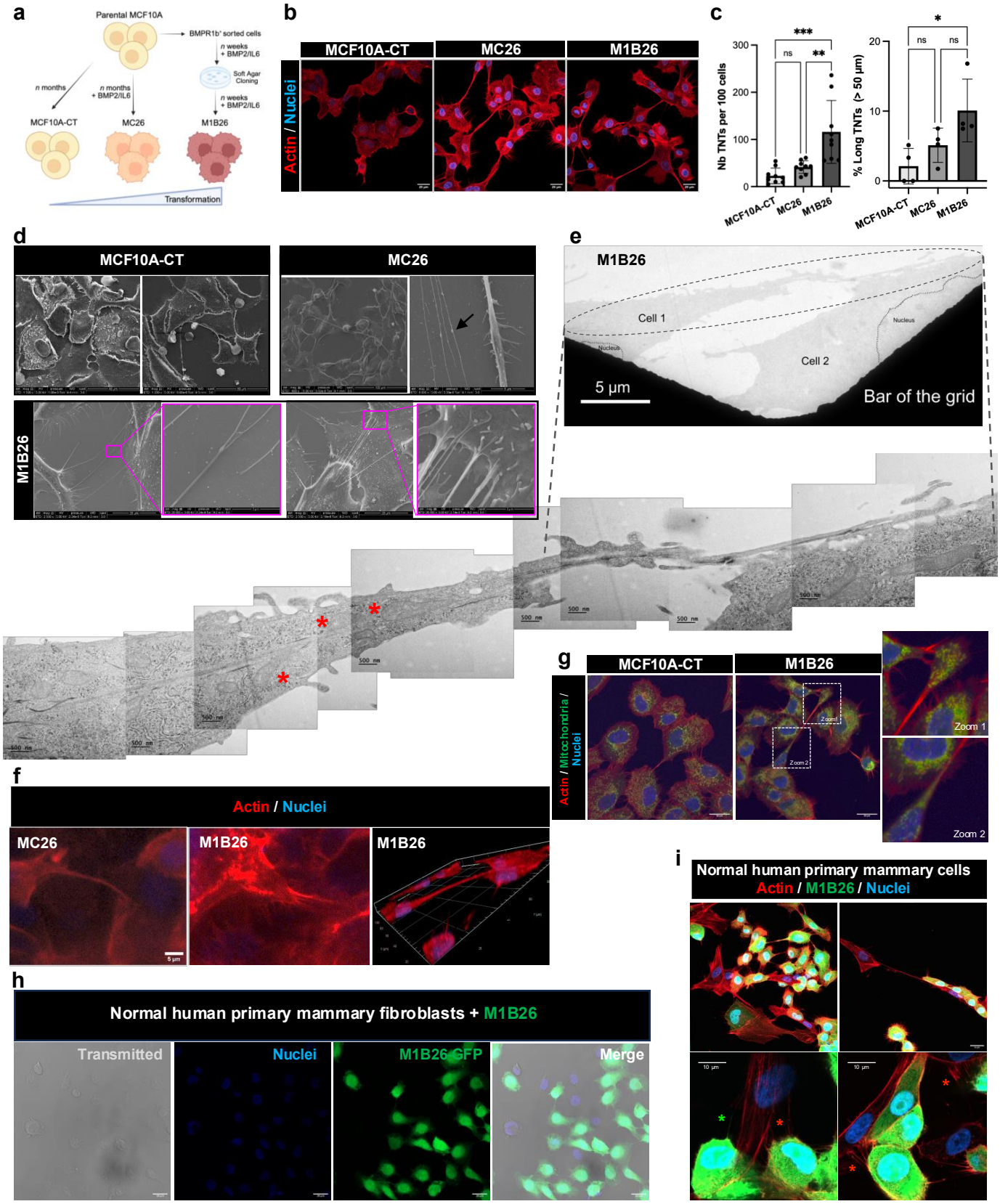
a
Parental MCF10A
BMPR1b+ sorted cells
n weeks + BMP2/IL6
Soft Agar Cloning
n months
n months + BMP2/IL6
n weeks + BMP2/IL6
MCF10A-CT
MC26
M1B26
Transformation
b
MCF10A-CT
MC26
M1B26
Actin / Nuclei
c
Nb TNTs per 100 cells
% Long TNTs (> 50 µm)
***
**
ns
*
MCF10A-CT
MC26
M1B26
d
MCF10A-CT
MC26
M1B26
e
M1B26
Cell 1
Cell 2
Nucleus
5 µm
Bar of the grid
500 nm
g
MCF10A-CT
M1B26
Actin / Mitochondria / Nuclei
Zoom 1
Zoom 2
f
Actin / Nuclei
MC26
M1B26
M1B26
5 µm
i
Normal human primary mammary cells
Actin / M1B26 / Nuclei
10 µm
h
Normal human primary mammary fibroblasts + M1B26
Transmitted
Nuclei
M1B26 GFP
Merge

1

Cuella Martin *et al* Figure 2

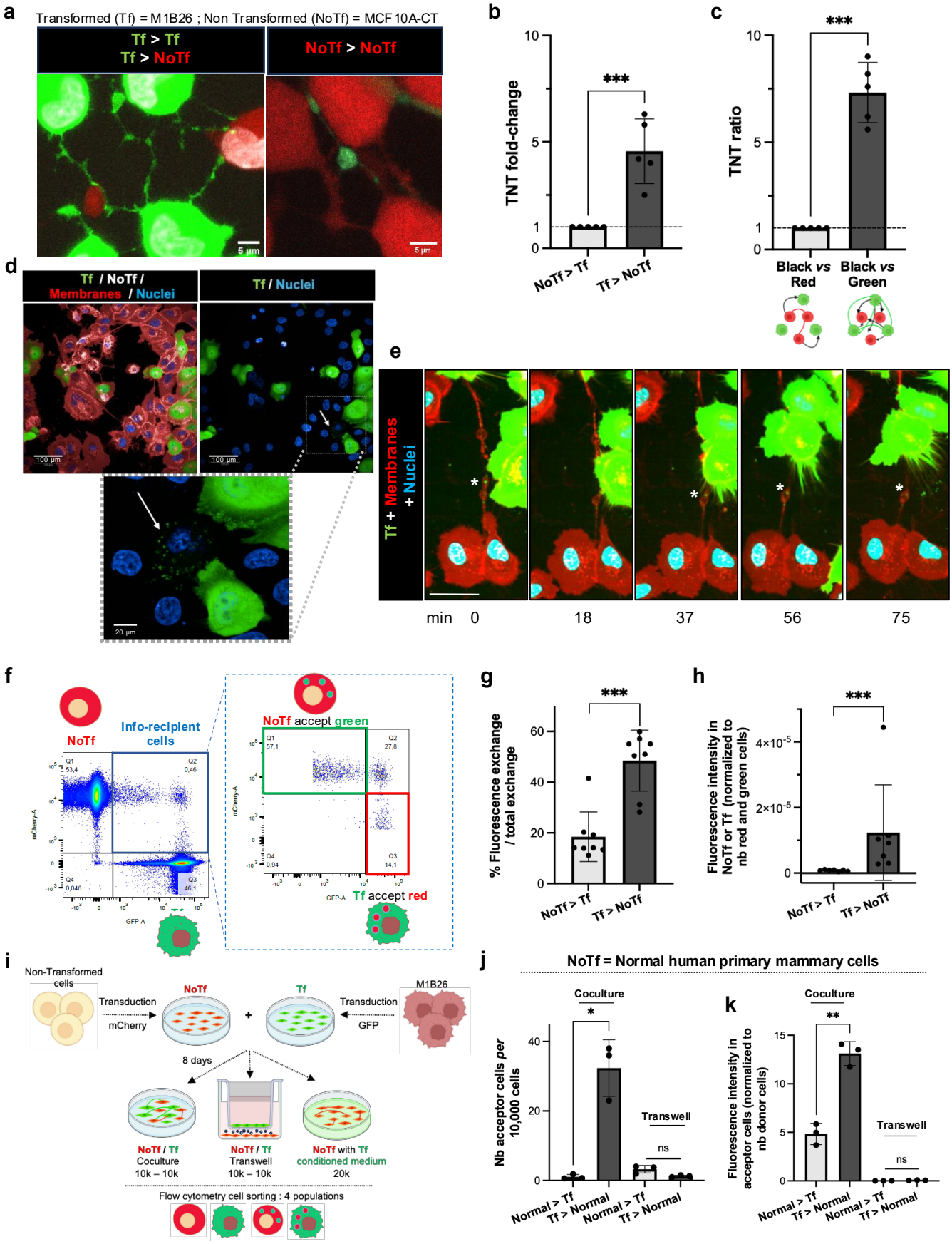

1

Cuella Martin *et al* Figure 3

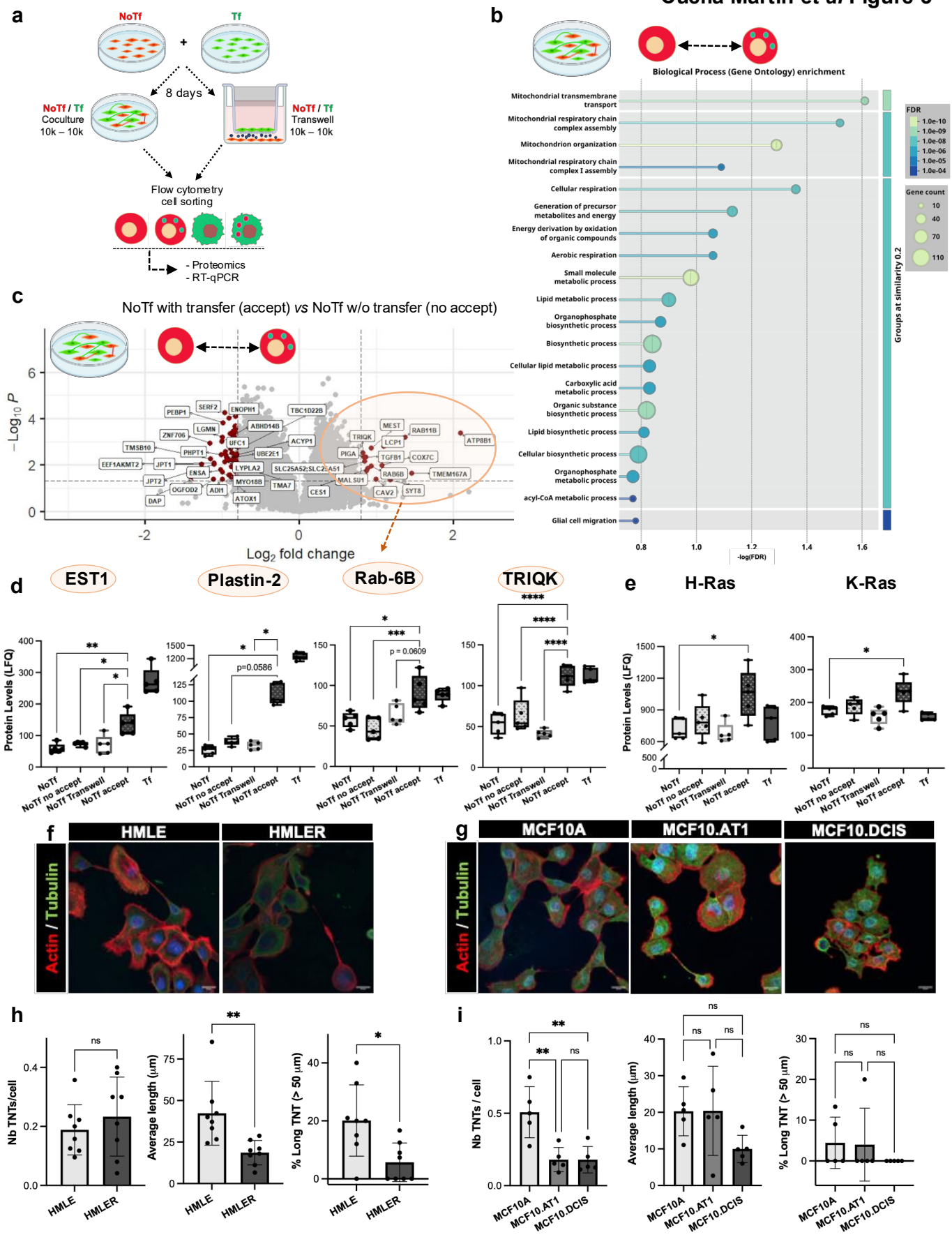

1

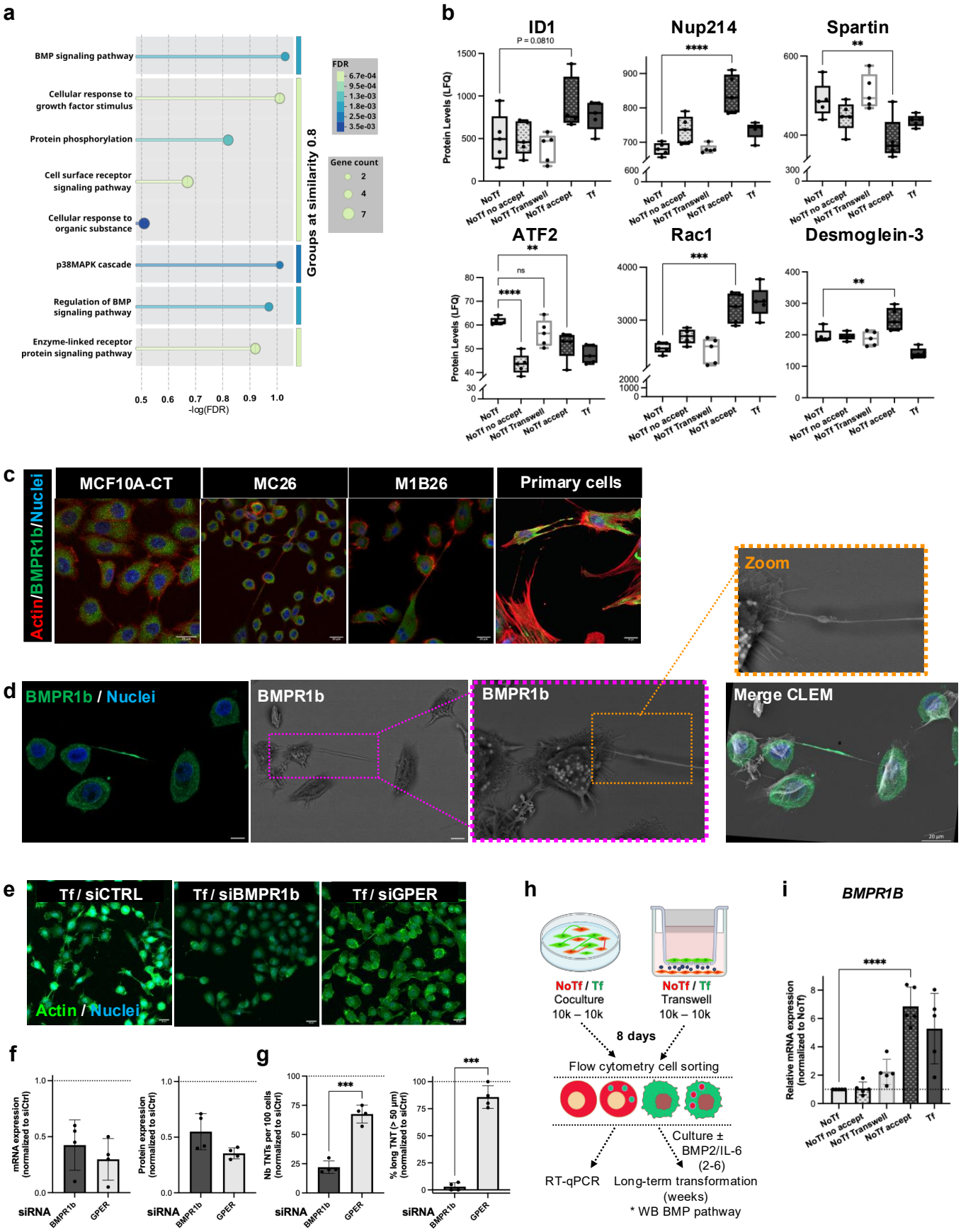
a
BMP signaling pathway
Cellular response to growth factor stimulus
Protein phosphorylation
Cell surface receptor signaling pathway
Cellular response to organic substance
p38MAPK cascade
Regulation of BMP signaling pathway
Enzyme-linked receptor protein signaling pathway
Groups at similarity 0.8
FDR
6.7e-04
9.5e-04
1.3e-03
1.8e-03
2.5e-03
3.5e-03
Gene count
2
4
7
0.5 0.6 0.7 0.8 0.9 1.0
-log(FDR)
b
ID1
P = 0.0810
Nup214
Spartin
ATF2
Rac1
Desmoglein-3
Protein Levels (LFQ)
NoTf
NoTf no accept
NoTf Transwell
NoTf accept
Tf
c
Actin/BMPR1b/Nuclei
MCF10A-CT
MC26
M1B26
Primary cells
Zoom
d
BMPR1b / Nuclei
BMPR1b
Merge CLEM
e
Tf / siCTRL
Tf / siBMPR1b
Tf / siGPER
Actin / Nuclei
f
mRNA expression (normalized to siCtrl)
Protein expression (normalized to siCtrl)
siRNA
BMPR1b
GPER
g
Nb TNTs per 100 cells (normalized to siCtrl)
% long TNT (> 50 µm) (normalized to siCtrl)
h
NoTf / Tf
Coculture
10k – 10k
NoTf / Tf
Transwell
10k – 10k
8 days
Flow cytometry cell sorting
Culture ± BMP2/IL-6 (2-6)
RT-qPCR
Long-term transformation (weeks)
* WB BMP pathway
i
BMPR1B
Relative mRNA expression (normalized to NoTf)

1

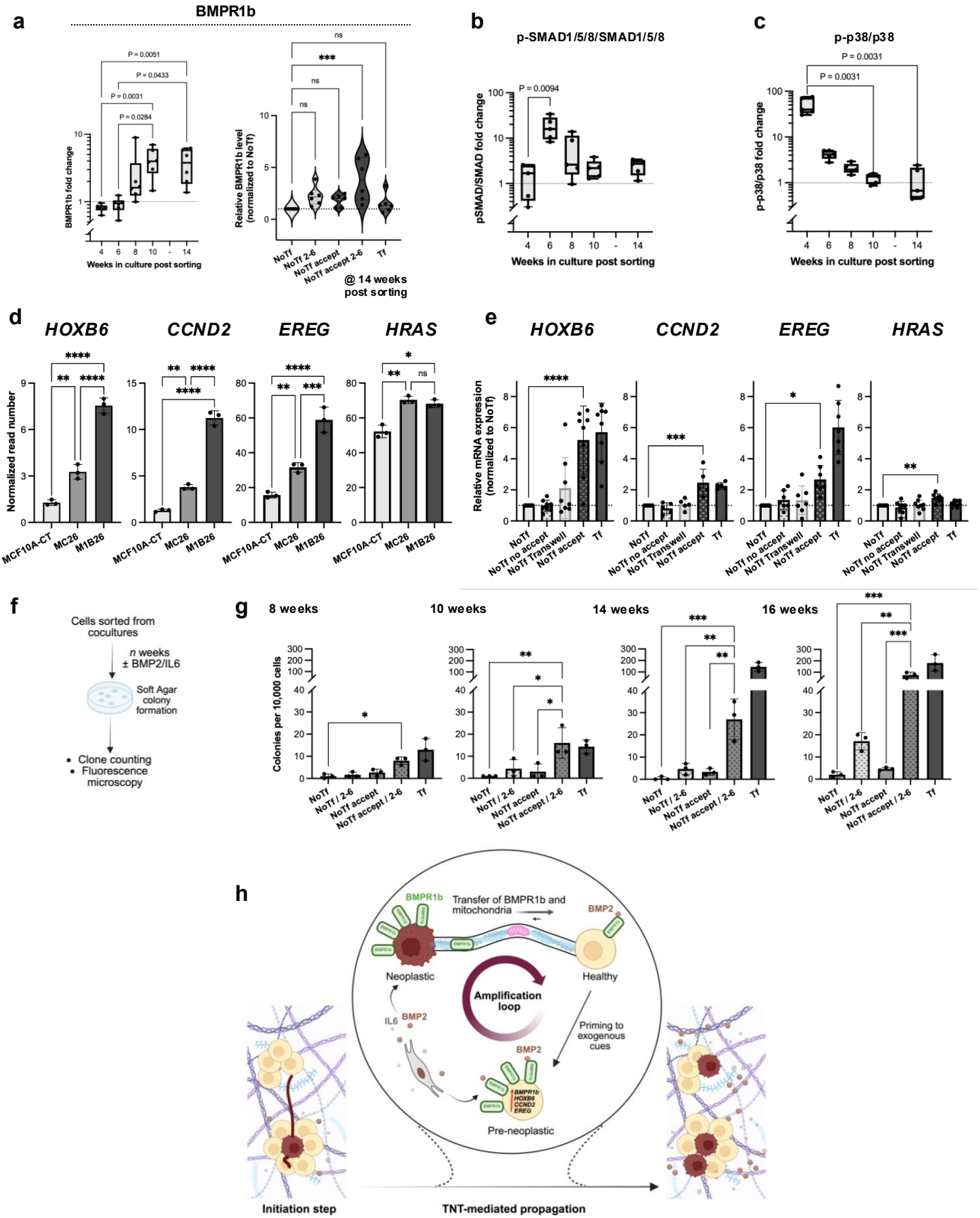
a
BMPR1b
P = 0.0051
P = 0.0433
P = 0.0031
P = 0.0284
BMPR1b fold change
Weeks in culture post sorting
ns
***
ns
ns
Relative BMPR1b level (normalized to NoTf)
NoTf
NoTf 2-6
NoTf accept
NoTf accept 2-6
Tf
@ 14 weeks post sorting
b
p-SMAD1/5/8/SMAD1/5/8
P = 0.0094
pSMAD/SMAD fold change
Weeks in culture post sorting
c
p-p38/p38
P = 0.0031
P = 0.0031
p-p38/p38 fold change
Weeks in culture post sorting
d
HOXB6
CCND2
EREG
HRAS
Normalized read number
MCF10A-CT
MC26
M1B26
e
HOXB6
CCND2
EREG
HRAS
Relative mRNA expression (normalized to NoTf)
NoTf
NoTf no accept
NoTf Transwell
NoTf accept
Tf
f
Cells sorted from cocultures
n weeks ± BMP2/IL6
Soft Agar colony formation
Clone counting
Fluorescence microscopy
g
8 weeks
10 weeks
14 weeks
16 weeks
Colonies per 10,000 cells
NoTf
NoTf / 2-6
NoTf accept
NoTf accept / 2-6
Tf
h
BMPR1b
Transfer of BMPR1b and mitochondria
BMP2
Neoplastic
Healthy
Amplification loop
IL6
BMP2
Priming to exogenous cues
BMP2
↑BMPR1b
↑HOXB6
↑CCND2
↑EREG
Pre-neoplastic
Initiation step
TNT-mediated propagation

1